Technical Note	LIGO-T1200008–v3	2012/05/13

Comparison of Quantum Limits in Interferometer Topologies for 3$^{\rm rd}$ Generation LIGO

Haixing Miao, Huan Yang, Rana Adhikari, and Yanbei Chen

California Institute of Technology
LIGO Project, MS 18-34
Pasadena, CA 91125
Phone (626) 395-2129
Fax (626) 304-9834
E-mail: info@ligo.caltech.edu

Massachusetts Institute of Technology
LIGO Project, Room NW22-295
Cambridge, MA 02139
Phone (617) 253-4824
Fax (617) 253-7014
E-mail: info@ligo.mit.edu

LIGO Hanford Observatory
Route 10, Mile Marker 2
Richland, WA 99352
Phone (509) 372-8106
Fax (509) 372-8137
E-mail: info@ligo.caltech.edu

LIGO Livingston Observatory
19100 LIGO Lane
Livingston, LA 70754
Phone (225) 686-3100
Fax (225) 686-7189
E-mail: info@ligo.caltech.edu

Contents

1 Introduction

The 2$^{\text{nd}}$ generation detectors, which are now being assembled (Advanced LIGO, Advanced Virgo, and KAGRA), are expected to be limited by quantum noise over nearly the entire GW band (10 - 10000 Hz). By quantum noise, we refer to the ground state fluctuations of the EM field which beat with the laser field to produce shot noise and radiation pressure noise.

To upgrade those detectors it is essential to reduce this quantum noise. There are several configurations that have been proposed within the community [1]. They generally fall into the following four categories:

- injection of squeezed light with a phase shifting filter cavity

- frequency dependent readout quadrature (a.k.a. variational readout)

- using coherent feedback to modify the dynamics of the test masses, e. g., the optical spring effect associated with the detuned signal recycling

- injecting multiple carrier fields

They all require, to a certain extent, introducing additional optics and increasing the complexity of the detectors. In this technical note we include realistic losses and quantitatively compare these configurations using the same baseline interferometer configuration.

We numerically optimize the sensitivity of the different configurations, which, following the convention of the LSC Instrument Science white paper [2], we call LIGO3, with the following cost function:

$$\mathcal{C}(\boldsymbol{x}) = \int_{f_{\min}}^{f_{\max}} \mathrm{d} \log f \, \log \left[\frac{h_{\text{AdvLIGO}}}{h_{\text{LIGO3}}(\boldsymbol{x})} \right]. \tag{1}$$

Here $[f_{\min}, f_{\max}]$ is the frequency span with $f_{\min} = 10\text{Hz}$ and $f_{\max} = 4040\text{Hz}$ for the optimization; $\boldsymbol{x}$ are the set of parameters that we want to optimize; h_{AdvLIGO} is the design sensitivity of AdvLIGO; and h_{LIGO3} is the sensitivity of the advanced configuration. Notice that the integration variable is $\log f$ instead of f, which means that we want to maximize the improvement over AdvLIGO in the log-log scale. We have considered the following configurations:

1. *frequency dependent squeeze angle*—injecting squeezed light with an optical filter cavity [3]

2. *frequency dependent readout*—filtering the output with a cavity to measure appropriate quadratures at different frequencies [3, 4];

3. *speed-meter configurations*—measuring quantity that is proportional to the test mass speed at low frequencies [5, 6, 7, 8]

4. *long signal recycling cavity*—elongating the recycling cavity to have a frequency-dependent response in the signal-recycling cavity

5. *dual-carrier scheme*—introducing an additional carrier light to gain another readout channel [9];

6. *local-readout scheme*—being a special case of the dual-carrier scheme in which the additional carrier is anti-resonant in the arm cavity and resonant in the power-recycling cavity [10].

These configurations are not excluded from each other and can be combined in different ways. In particular, we not only consider them standalone, but also combine (i) and (ii)—input and output filter cavities—with other schemes.
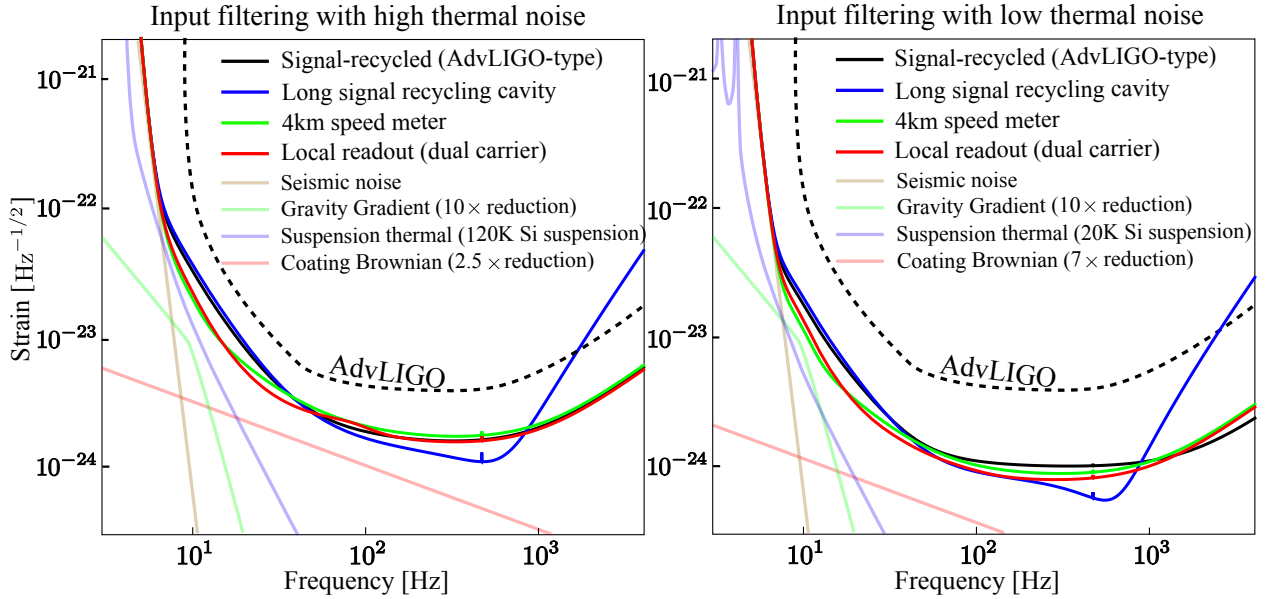
Figure 1: Plot showing the optimized total noise spectrum for different configurations with frequency-dependent squeezing (input filtering). The left (right) one assumes high (low) thermal noise.

The optimization results are shown in Fig. 1 and Fig 2, where we plot the total noise spectrum (the quantum noise + the classical noises) for different configurations with frequency dependent squeezing (input filtering) and variational readout (output filtering). In producing the left ones in these two figures, we assume a moderate reduction in the thermal noise and the same mass and optical power as those for AdvLIGO. In producing the right ones in these figures, we assume a more optimistic reduction in the thermal noise and, in addition, the test mass to be 150 kg and a maximal optical power to be 3 MW. As we can see, by adding just one filter cavity to the signal-recycled interferometer (AdvLIGO topology), we can already obtain a broadband improvement over AdvLIGO. Further low-frequency enhancement can be achieved by applying either the speed meter or the local-readout (dual-carrier Michelson) scheme.

The outline of this note goes as follows: in Sec. 2, we introduce the topologies and features of different configurations that we are about to compare; in Sec. 3, we will compare their broadband sensitivity by optimizing their parameters under the same cost function defined in Eq. (1); in Sec. 5, we will summarize our main results. In the appendices, we present a
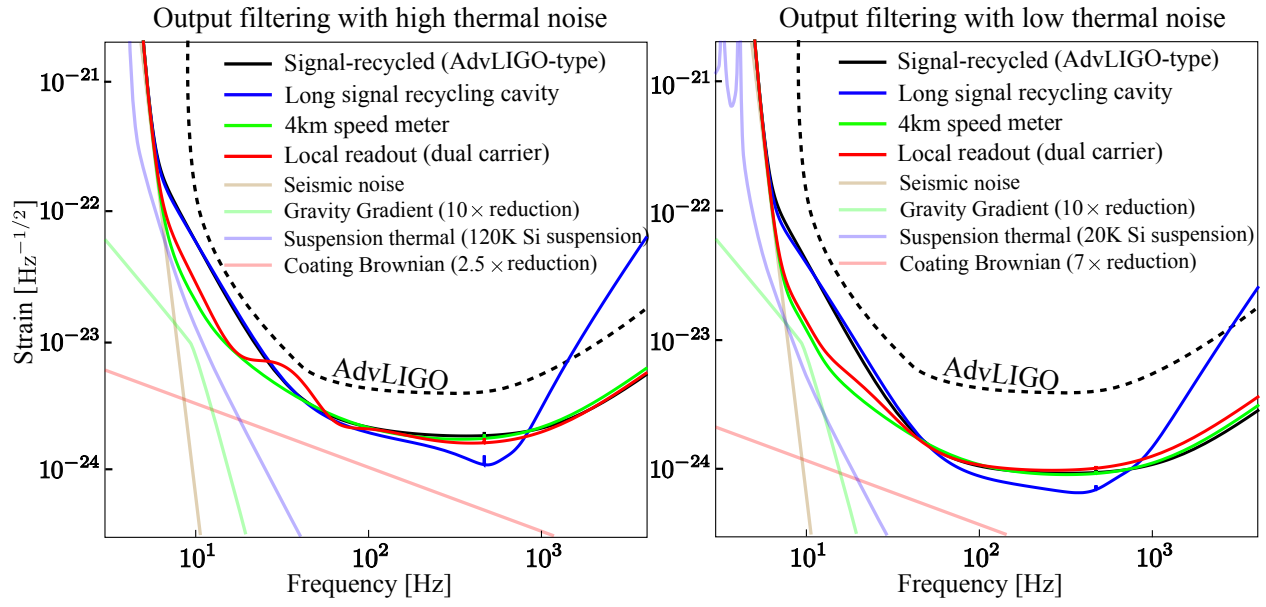
Figure 2: Plot showing the optimization results for different configuration with variational readout (output filtering). The left (right) one assumes high (low) thermal noise.

table of the optimal optical parameters, summarize the basics of quantum noise calculation, and also define the variables used here relative to the previous theoretical papers on the topic.

2 Optical Topologies

In this section, we describe the optical topologies that we compare in Section 3. The quantum noise spectral density of these topologies are evaluated by using the standard input-output formalism, and we give a brief introduction to it in the App. B. With the additional optics, the topologies to be considered have different input-output relations from that of a tuned signal-recycling interferometer, e.g., the scheme for the advanced LIGO, and thus different quantum noise spectra.

2.1 Frequency-dependent squeezing—input filtering
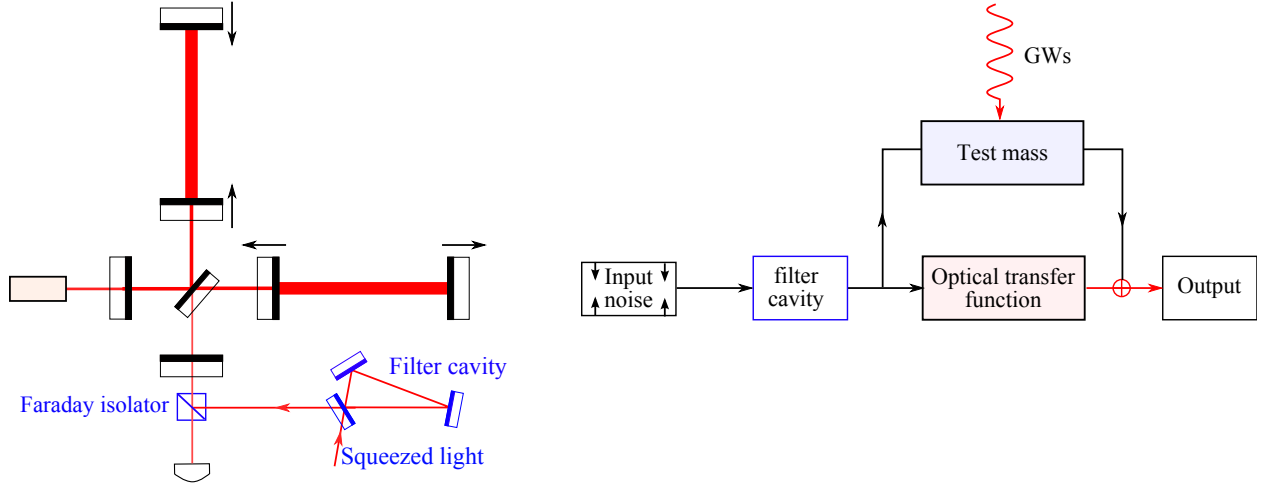
Figure 3: Schematics showing the frequency-dependent squeezing scheme (left) and its associated flow chart (right).

The first scheme is frequency-dependent squeezing. Unlike the vacuum state of which the spectral density matrix is an identity matrix, the squeezed light has the following noise spectral density matrix:

$$\left[\begin{array}{cc} S_{11} & S_{12} \\ S_{21} & S_{22} \end{array} \right] = \left[\begin{array}{cc} \cosh 2r - \sinh 2r \cos 2\varphi & -\sinh 2r \sin 2\varphi \\ -\sinh 2r \sin 2\varphi & \cosh 2r - \sinh 2r \cos 2\varphi \end{array} \right] \tag{2}$$

where r is called the squeezing factor (10 dB squeezing means that $e^{2r} = 10$) and φ is the squeezing angle, e.g., when $\varphi = \pi/2$ and $r > 0$, $S_{11} = e^{2r}, S_{12} = S_{21} = 0, S_{22} = e^{-2r}$, the fluctuation in the phase quadrature is squeezed compared with that of the vacuum (which is equal to 1). Frequency-dependent squeezing, as shown schematically in Fig. 3, utilizes an optical cavity to rotate the amplitude and phase quadratures, or equivalently the squeezing angle, in a frequency-dependent way. Specifically, the amplitude and phase quadratures, a_1 and a_2, after being filtered by the optical cavity are:

$$\left[\begin{array}{c} a_1'(\Omega) \\ a_2'(\Omega) \end{array} \right] = e^{i(\alpha_+ - \alpha_+)/2} \left[\begin{array}{cc} \cos \frac{\alpha_+ + \alpha_-}{2} & -\sin \frac{\alpha_+ + \alpha_-}{2} \\ \sin \frac{\alpha_+ + \alpha_-}{2} & \cos \frac{\alpha_+ + \alpha_-}{2} \end{array} \right] \left[\begin{array}{c} a_1(\Omega) \\ a_2(\Omega) \end{array} \right] \tag{3}$$

and $\alpha_\pm$ is defined as:

$$e^{i\alpha_\pm} \equiv \frac{i\gamma \mp \Omega - \Delta}{i\gamma \pm \Omega - \Delta}, \tag{4}$$

where Δ and γ are the detune and bandwidth of the filter cavity, respectively. The quadratures undergo a frequency-dependent rotation of $(\alpha_+ + \alpha_-)/2$, and if the frequency dependency is appropriate, one can rotate the squeezing angle such that the quantum noise spectrum is reduced by an overall factor that is equal to e^{2r}, namely (in the case of the tuned interferometer)

$$S_h(\Omega) = e^{-2r} \left[\mathcal{K}(\Omega) + \frac{1}{\mathcal{K}(\Omega)} \right] \frac{h_{\text{SQL}}^2}{2}. \tag{5}$$

For illustration, in Fig. 4, we show the resulting noise spectrum in the ideal case without optical loss (the effect of the optical loss will be discussed later). As we can see, the squeezing angle rotates in such a way that at low frequencies the fluctuation in the amplitude quadrature is squeezed—thus reducing the radiation-pressure noise, while at high frequencies the phase quadrature is squeezed—thus reducing the shot noise. In order to achieve the desired rotation of squeezing angle, the filter cavity needs to have a bandwidth that is comparable to the detection bandwidth—this indicates a high-finesse cavity is necessary if the cavity length is short. The specification for the filter cavity can almost be analytically calculated by using the method outlined in [7]. To account for optical loss accurately, we use numerical methods to optimize the parameters of the filter cavity.
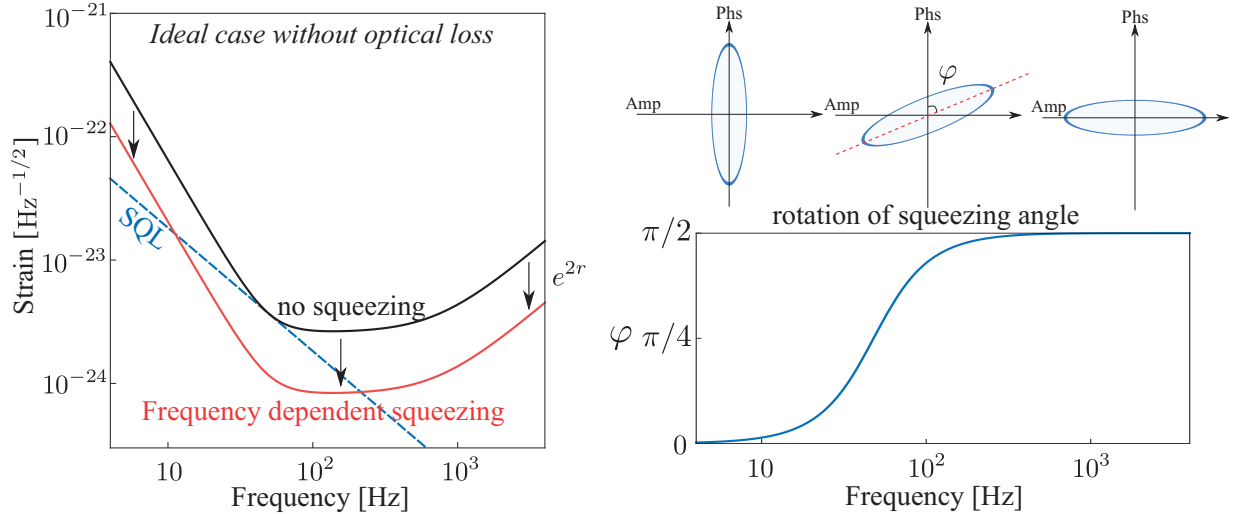
Figure 4: Noise spectrum for frequency-dependent squeezing (left) and rotation of the squeezing angle (right).

2.2   Frequency Dependent Readout—Output Filtering

A close related counterpart to the input filtering is the variational readout, and as shown schematically in Fig. 5, it uses an optical cavity to filter the detector output which allows one
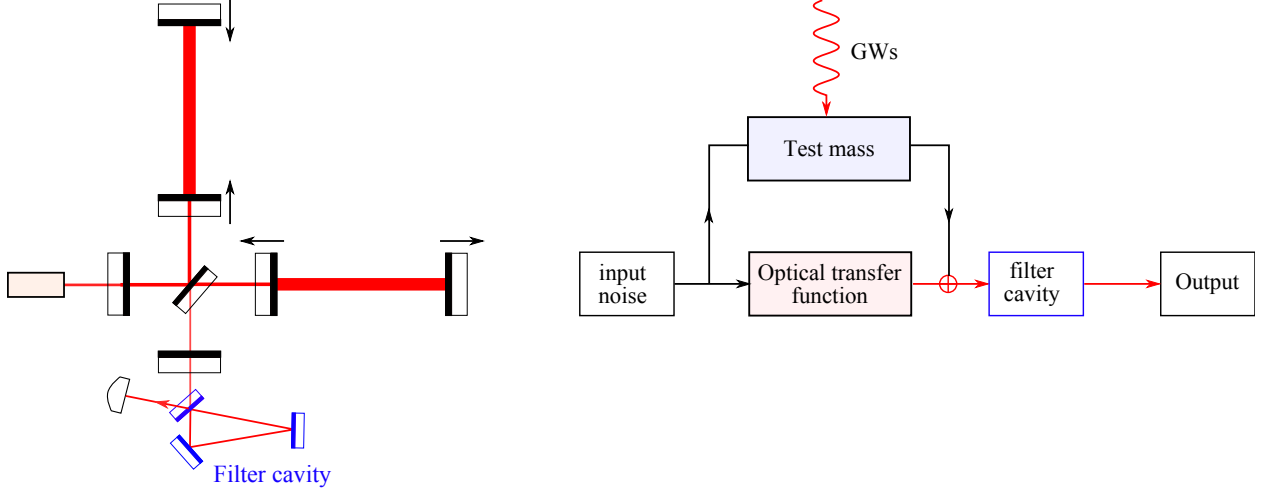
Figure 5: Schematics showing the frequency dependent (or variational) readout scheme (left) and its associated flow chart (right).

to measure different optical quadratures at different frequencies. The filter cavity has the same functionality as in the case of the frequency-dependent squeezing—the only difference is that it rotates the optical quadratures of the output instead of input. In the ideal case, this scheme can coherently cancel the radiation-pressure noise at low-frequencies [3]. To illustrate how this works, we use the tuned interferometer, of which the input-output relation is given by Eq. (32). If we choose a proper local-oscillator phase and make the quadrature angle to be ζ that is not equal to zero (phase quadrature), we have [cf. Eq. 32]:

$$b_\zeta(\Omega) = b_1(\Omega)\sin\zeta + b_2(\Omega)\cos\zeta$$

$$= e^{2i\phi}[\sin\zeta - \mathcal{K}(\Omega)\cos\zeta]a_1(\Omega) + e^{2i\phi}\cos\zeta\, a_2(\Omega) + e^{i\phi}\cos\zeta\sqrt{2\mathcal{K}(\Omega)}\frac{h(\Omega)}{h_{\text{SQL}}}. \quad (6)$$

Here the first term, proportional to a_1, is the radiation pressure noise; the second term, proportional to a_2, is the shot noise; the third term is the signal. As we can see, if the quadrature angle ζ in the following frequency dependency way:

$$\tan\zeta = \mathcal{K}(\Omega), \quad (7)$$

the first radiation-pressure noise term would be canceled, and give rise to a shot-noise only sensitivity. Since the phase for the local oscillator is usually fixed, before beating with the local oscillator we need to rotate the output quadratures with a filter cavity to achieve such a frequency-dependent quadrature readout.

The resulting noise spectrum for this scheme is simply:

$$S_h(\Omega) = \frac{1}{\mathcal{K}(\Omega)}\frac{h_{\text{SQL}}^2}{2}. \quad (8)$$

If we simultaneously inject phase squeezed light, we will have:

$$S_h(\Omega) = \frac{e^{-2r}}{\mathcal{K}(\Omega)}\frac{h_{\text{SQL}}^2}{2}. \quad (9)$$

In Fig. 6, we plot the noise spectrum in the ideal lossless case with the low-frequency radiation-pressure noise completely evaded. In reality, due to the presence of optical loss, such a cancelation cannot be perfect. In the numerical optimization, we will take into account the optical loss and optimize the parameters for the filter cavity.
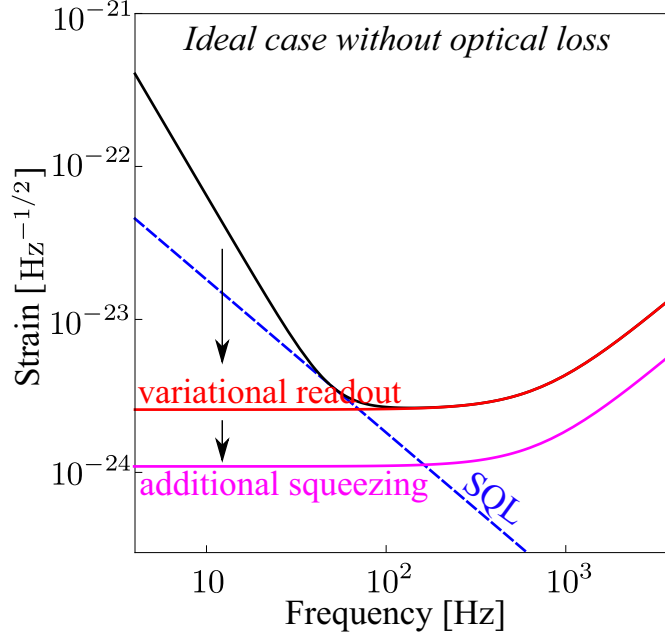
Figure 6: Plot showing the noise spectrum for the variational readout scheme (red curve) and with additional phase squeezed light injection (purple curve).

2.3 The Effects of Optical Losses

In the previous two subsections, we introduced the frequency-dependent squeezing (input filtering) and the variational readout (output filtering). For illustration, we assumed the ideal case without any optical loss. Even though we will include realistic optical loss in the numerical optimization, it is worth mentioning briefly how the optical loss influences the performance of these two schemes, as we will combine them with other advanced schemes discussed in later subsections.

Frequency-dependent squeezing.—For the frequency-dependent squeezing scheme, the optical loss introduces additional (vacuum) noise that is uncorrelated with the input squeezed light:

$$a'_1 = \sqrt{\eta}\, n_1 + \sqrt{1-\eta}\, a_1, \tag{10}$$

$$a'_2 = \sqrt{\eta}\, n_2 + \sqrt{1-\eta}\, a_2, \tag{11}$$

where η quantifies the optical loss—one ppm loss means that $\eta = 10^{-6}$—and $n_{1,2}$ are associated noises in the amplitude and phase quadratures. These noises will deteriorate the squeezing. For instance, the amplitude squeezed light originally has $S_{11} = e^{-2r}$ with $r > 0$. Due to the optical loss, from Eq. 10, it becomes:

$$S'_{11} = (1-\eta)e^{-2r} + \eta. \tag{12}$$

For a completely lossy case with $\eta = 1$, we have $S_{11} = 1$ and the squeezing simply vanishes.

The squeezed light at different frequencies experiences different optical loss of the filter cavity. The low-frequency part enters the cavity and circulates for multiple times, while the high-frequency part barely enters the cavity. Therefore, the optical loss affects the low-frequency part most significantly. In terms of noise spectrum, we approximately have (again assume the tuned interferometer):

$$S_h(\Omega) = \left\{ [(1-\eta)e^{-2r} + \eta]\mathcal{K}(\Omega) + \frac{e^{-2r}}{\mathcal{K}(\Omega)} \right\} \frac{h_{\mathrm{SQL}}^2}{2}, \tag{13}$$

in contrast to Eq. (5). Compared with ideal frequency-dependence squeezing case, the low-frequency radiation-pressure noise increases due to the optical loss and the high-frequency shot noise remains almost the same.

Variational readout.—For variational readout, the additional noise introduced by the optical loss influences the output and modifies the input-output relation as (use the tuned interferometer for illustration [cf. Eq. (32)]):

$$\begin{bmatrix} b_1' \\ b_2' \end{bmatrix} = \sqrt{\eta} \begin{bmatrix} n_1 \\ n_2 \end{bmatrix} + \sqrt{1-\eta}\, e^{2i\phi} \begin{bmatrix} 1 & 0 \\ -\mathcal{K} & 1 \end{bmatrix} \begin{bmatrix} a_1 \\ a_2 \end{bmatrix} + \sqrt{1-\eta}\, e^{i\phi} \begin{bmatrix} 0 \\ \sqrt{2\mathcal{K}} \end{bmatrix} \frac{h}{h_{\mathrm{SQL}}}. \tag{14}$$

Due to the presence of uncorrelated noise, the condition in Eq. (??) not longer provides radiation-pressure noise cancelation. By optimizing the quadrature angle ζ, for the tuned interferometer with phase squeezed light injection, one can find the optimal sensitivity, in contrast to Eq. (9), reads:

$$S_h(\Omega) = \left[\frac{\epsilon\, e^{2r}\mathcal{K}(\Omega)}{\epsilon + e^{2r}} + \frac{e^{-2r} + \epsilon}{\mathcal{K}(\Omega)} \right] \frac{h_{\mathrm{SQL}}^2}{2} \tag{15}$$

with $\epsilon \equiv \eta/(1-\eta) \approx \eta$.

Comparison.—Here we make a comparison between these two schemes in terms of the significance of the optical loss. We only focus at the low-frequency part of the sensitivity, as mentioned earlier that the optical loss of the filter cavity is only important at low frequencies. Therefore, we just need to compare the numerical factor of the radiation-pressure noise: $(1-\eta)e^{-2r} + \eta$ for the frequency-dependent squeezing scheme and $\epsilon\, e^{2r}/(\epsilon + e^{2r})$ for the variational-readout scheme. In Fig. 7, we plot these two factors as a function of the round-trip loss of the cavity. As we see, the variational-readout scheme is more susceptible to the optical loss, but it has a better performance compared with the frequency-dependent squeezing if the optical loss can be low.

2.4   Long signal-recycling cavity

In this subsection, we will discuss the long signal-recycling cavity scheme. As shown in Fig. 8, the signal recycling mirror is moved further away from the beam splitter compared with the AdvLIGO configuration. In the usual case when the beam splitter and the signal-recycling mirror are close to each other, the signal-recycling cavity is relatively short (order of 10 meters) and one can ignore the phase shift difference between different sidebands with
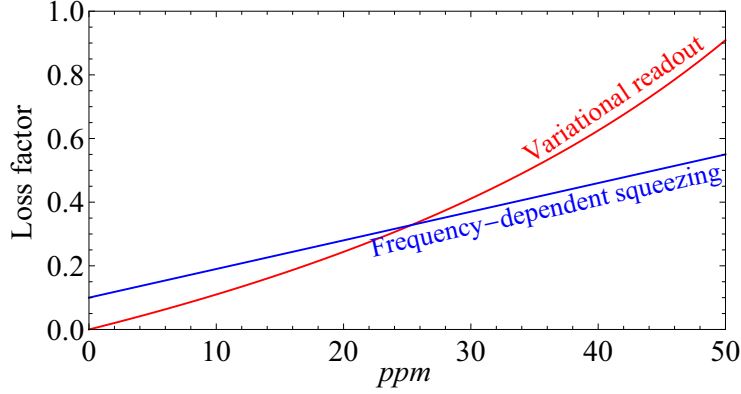
Figure 7: Plot showing the loss factor as a function of round-trip loss of the cavity for two schemes (the smaller is the loss factor, the better is the performance). The total optical loss η is equal to the round-trip loss multiplied by the number of bounce. Here we have assumed a finesse to be around 1.5×10^4.
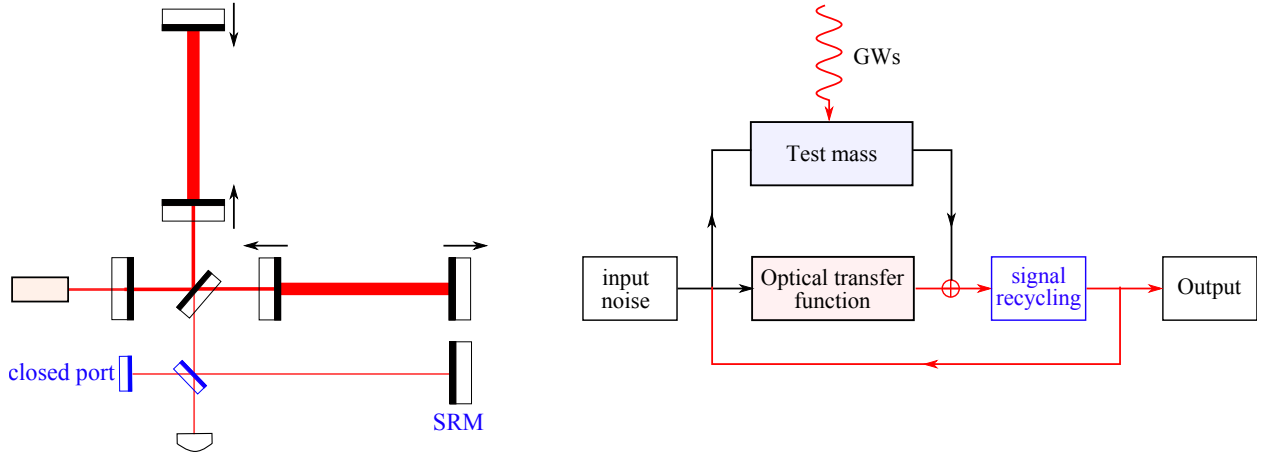
Figure 8: Schematics showing the long signal-recycling cavity scheme (left) and its associated flow chart (right). The signal-recycling mirror coherently reflects back the signal, forming a feedback loop as indicated in the flow chart.

frequency ranging from 10 - 10000 Hz, namely $\Omega L_{\rm sr}/c \approx 0$ with $L_{\rm sr}$ being the signal-recycling cavity length. We can therefore treat the signal-recycling cavity as an effective compound mirror with complex transmissivity and reflectivity, which is the approach applied in Ref. [11]. With a long signal-recycling cavity, however, $\Omega L_{\rm sr}/c$ is not negligible and different sidebands pick up different phase shifts. Specifically, the transfer function matrix for the quadratures due to the free propagation in the signal-recycling cavity is given by:

$$e^{i\Omega\tau_{\rm sr}} \left[\begin{array}{cc} \cos\Delta\tau_{\rm sr} & -\sin\Delta\tau_{\rm sr} \\ \sin\Delta\tau_{\rm sr} & \cos\Delta\tau_{\rm sr} \end{array} \right] \tag{16}$$

with $\tau_{\rm sr} \equiv L_{\rm sr}/c$ and Δ the detune frequency of the signal-recycling cavity. After taking into account this fact, one can then apply the standard procedure to derive the input-output relation for this scheme. The final expression is quite lengthy and not illuminating, and we will not show it here. We will evaluate its noise spectrum numerically.

2.5 Speed meter

The motivation for speed meter arises from the perspective of viewing the gravitational-wave detector as a quantum measurement device. Normally, we measure the test mass position at different times to infer the gravitational-wave signal. However, position is not a conserved dynamical quantity of the test mass which is treated as a free mass in the theoretical model. According to the quantum measurement theory [12], such a measurement process will inevitably introduce additional back action and perturb the test mass motion. In the context here, the back action is the radiation-pressure noise. In order to evade the back action, one needs to measure the conserved dynamical quantity of the test mass—the momentum or the energy. Since the momentum is proportional to the speed, that is why speed meter is ideal for measuring gravitational wave with no radiation-pressure noise [5].
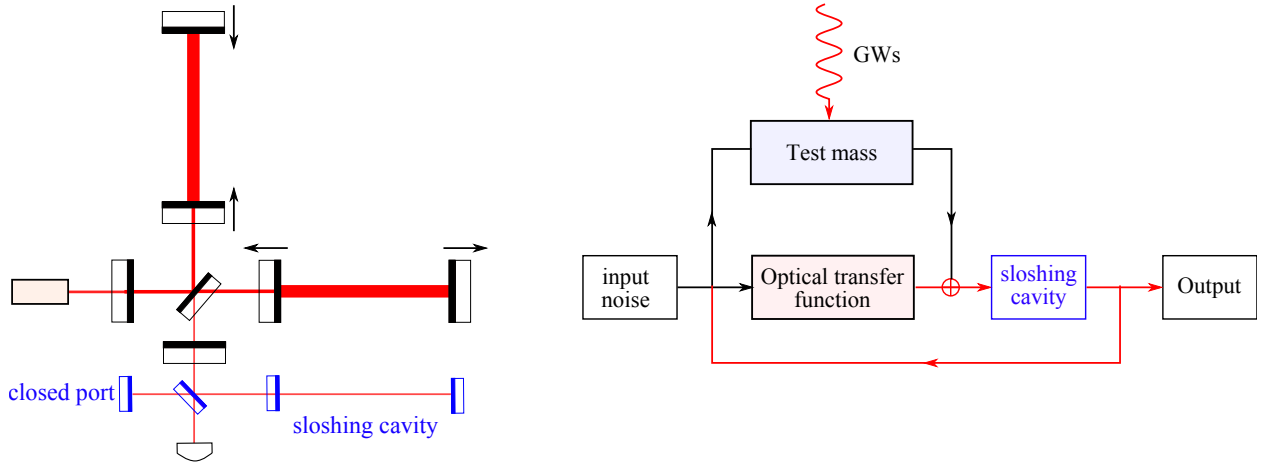
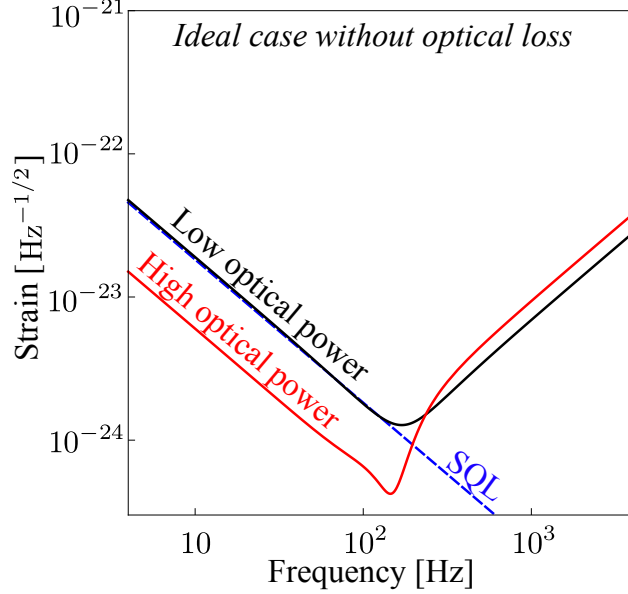**Figure 9:** Schematics showing the speed-meter configuration (left) and its flow chart (right).

There are several speed-meter configurations, e.g., the Sagnac interferometer [8] and a recent proposed scheme by using different polarizations [13]. In Fig. 9, we show one particular variant of them, which is proposed in Ref. [7]. It uses a sloshing cavity. We can gain a qualitative understanding of how such a scheme allows us to measure the speed of the test mass. Basically, the information of test mass position at an early moment is stored in the sloshing cavity, and it coherently superposes (but with a minus sign due to the phase shift in the tuned cavity) with the output of the interferometer which contains the current test mass position. The sloshing happens at a frequency that is comparable to the detection frequency, and the superposed output is, therefore, equal to the derivative of the test-mass position, i.e., the speed.

The detail of this scheme has been presented in Ref. [7], in particular the input-output relation which will be used in the numerical optimization. At this moment, we just show the resulting quantum-noise spectrum for this scheme:

$$S_h(\Omega) = \frac{1}{\mathcal{K}_{\mathrm{sm}}(\Omega)} \frac{h_{\mathrm{SQL}}^2}{2} \tag{17}$$

with

$$\mathcal{K}_{\mathrm{sm}}(\Omega) = \frac{16\omega_0 \gamma P_c}{mcL[(\Omega^2 - \omega_s^2)^2 + \gamma^2 \Omega^2]}. \tag{18}$$

Figure 10: Plot showing the noise spectrum for the speed-meter configuration for two different optical powers.

There is no radiation-pressure noise at low frequencies, and therefore the sensitivity is only limited by the amount of optical power that we have. This noise spectrum is shown in Fig. 10. The low-frequency spectrum has the same slope as the standard quantum limit, which is a unique feature of speed meter. When the optical is high enough, we can surpass the standard quantum limit.

One important characteristic frequency for this type of speed meter is the sloshing frequency ω_s, and it is defined as

$$\omega_s = \frac{c}{2}\sqrt{\frac{T_s}{L\,L_s}}, \tag{19}$$

where T_s is the power transmissivity for the front mirror of the sloshing cavity and L_s is the cavity length. To achieve a speed response in the detection band, this sloshing frequency needs to be around 100Hz. For a 4km arm cavity—$L = 4000$ and 100m sloshing cavity—$L_s = 100$, it requires the transmittance of the sloshing mirror to be

$$T_s \approx 30\,\mathrm{ppm}. \tag{20}$$

This puts a rather tight constraint on the optical loss of the sloshing cavity. To release such a constraint on the optical loss, we can use the fact that ω_s only depends on the ratio between the transmissivity of the sloshing mirror and the cavity length and we can therefore increase the cavity length.

2.6 Multiple Carrier Fields

In this section, we will introduce the multiple carrier light scheme, and in particular, we will focus on the dual-carrier case as shown schematically in Fig. 11. The additional carrier light provides us another readout channel. As these two carriers can have a very large
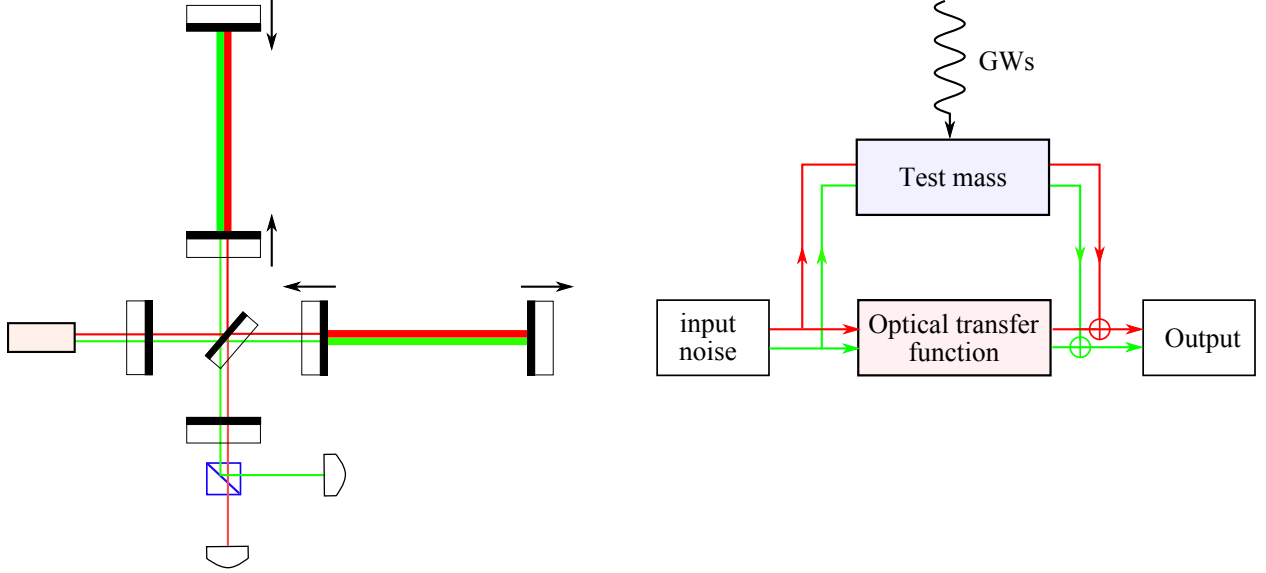
Figure 11: Schematics showing the dual-carrier scheme (left) and its flow chart (right).

frequency separation, we can in principle design the optics in such a way that they have different optical power and see different detune and bandwidth. In addition, they can be independently measured at the output. This allows us to gain a lot flexibilities and almost provides multiple interferometers but within the same set of optics.

These two optical fields are not completely independent, and they are coupled to each other as both act on the test masses and sense the test-mass motion (shown pictorially by the flow chart in Fig. 11). More explicitly, we can look at the input-output relation for this scheme in the simple case with both fields are tuned:

$$
\begin{bmatrix} b_1^{(A)} \\ b_2^{(A)} \\ b_1^{(B)} \\ b_2^{(B)} \end{bmatrix} = \begin{bmatrix} 1 & 0 & 0 & 0 \\ -\mathcal{K}_A & 1 & -\sqrt{\mathcal{K}_A \mathcal{K}_B} & 0 \\ 0 & 0 & 1 & 0 \\ -\sqrt{\mathcal{K}_A \mathcal{K}_B} & 0 & -\mathcal{K}_B & 1 \end{bmatrix} \begin{bmatrix} a_1^{(A)} \\ a_2^{(A)} \\ a_1^{(B)} \\ a_2^{(B)} \end{bmatrix} + \begin{bmatrix} 0 \\ \sqrt{2\mathcal{K}_A} \\ 0 \\ \sqrt{2\mathcal{K}_B} \end{bmatrix} \frac{h}{h_{\mathrm{SQL}}}, \tag{21}
$$

where we have ignored uninteresting phase factor $e^{i\phi}$ and we have introduced

$$
\mathcal{K}_A = \frac{16\,\omega_0^{(A)}\gamma_A P_c^{(A)}}{mLc\,\Omega^2(\Omega^2 + \gamma_A^2)}, \quad \mathcal{K}_B = \frac{16\,\omega_0^{(B)}\gamma_B P_c^{(B)}}{mLc\,\Omega^2(\Omega^2 + \gamma_B^2)}. \tag{22}
$$

The term $-\sqrt{\mathcal{K}_A \mathcal{K}_B}$ in the transfer function matrix indicates the coupling between these two optical fields, and it comes from the fact that the radiation-pressure noise from the first one is sensed by the second one and vise versa.

As mentioned earlier, because the frequency separation between them is much lager than the detection band, these two fields can be measured independently and give two outputs $b_\zeta^{(A)}$ and $b_\zeta^{(B)}$:

$$
b_\zeta^{(A)} = b_1^{(A)} \sin \zeta_A + b_2^{(A)} \cos \zeta_A, \quad b_\zeta^{(B)} = b_1^{(B)} \sin \zeta_B + b_2^{(B)} \cos \zeta_B. \tag{23}
$$

To achieve the optimal sensitivity, we need to combine them with the optimal filters $C_A(\Omega)$ and $C_B(\Omega)$, obtaining

$$b_\zeta^{\text{tot}}(\Omega) = C_A(\Omega)b_\zeta^{(A)}(\Omega) + C_B(\Omega)b_\zeta^{(B)}(\Omega). \tag{24}$$

In [9], the authors have shown the procedure for obtaining the optimal sensitivity and the associated optimal filters in the general case with multiple carriers. Here we plot the resulting noise spectrum. Given the input-output relation: $\boldsymbol{b} = \mathbf{M}\boldsymbol{a} + \boldsymbol{v}h$—a simplified vector form of Eq. (21), the noise spectrum that gives the optimal sensitivity is:
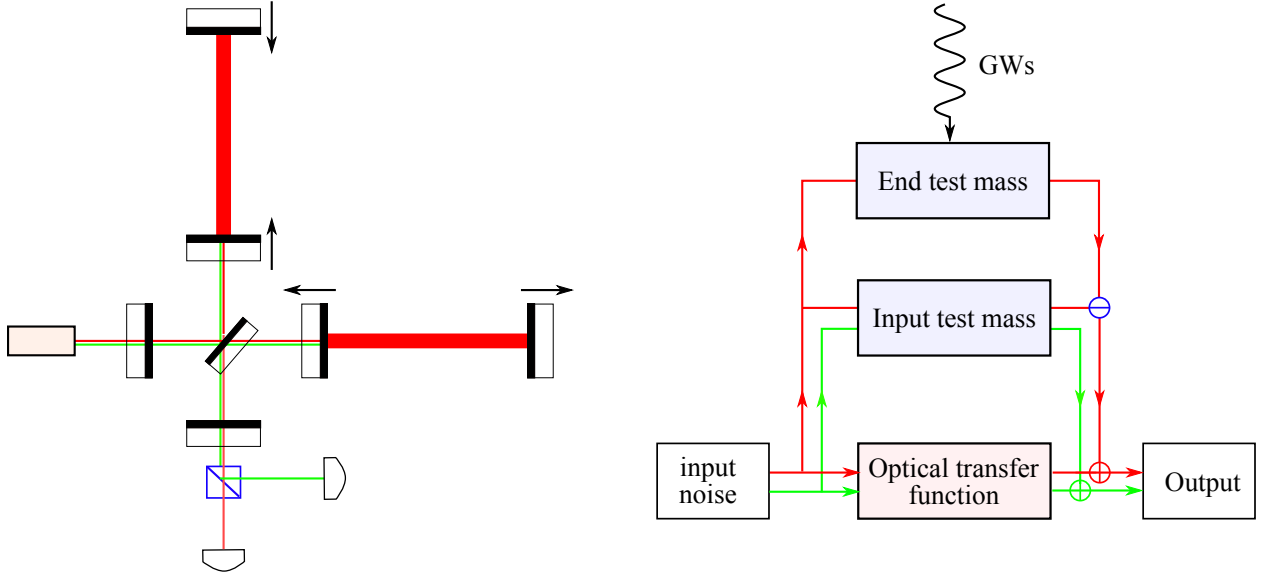
$$S_h(\Omega) = \left[\boldsymbol{v}^\dagger\mathbf{M}_{\text{hd}}^\dagger(\mathbf{M}_{\text{hd}}\mathbf{M}\,\mathbf{M}^\dagger\mathbf{M}_{\text{hd}}^\dagger)^{-1}\mathbf{M}_{\text{hd}}\boldsymbol{v}\right]^{-1}, \tag{25}$$

where we have defined:

$$\boldsymbol{M}_{\text{hd}} = \begin{bmatrix} \sin\zeta_A & \cos\zeta_A & 0 & 0 \\ 0 & 0 & \sin\zeta_B & \cos\zeta_B \end{bmatrix}. \tag{26}$$

This result is used for our numerical optimization in Sec. 3.

2.7 Local Readout

Figure 12: Diagram of the local-readout topology (left) and the resulting feedback loops (right).

In this subsection, we will discuss the local-readout scheme, as shown schematically in Fig. 12. It is actually a special case of the dual-carrier scheme mentioned in the pervious subsection— the second carrier light is only resonant in the power-recycling cavity and is anti-resonant in arm cavity (barely enters the arm cavity). Why we single this scheme out of the general dual-carrier scheme and give it a special name is more or less due to a historic reason. This scheme was first proposed in Ref. [10] and was motivated by trying to enhance the low-frequency sensitivity of a detuned signal-recycling interferometer, which is not as good as the tuned signal-recycling due to the optical-spring effect. The name—"local readout"—originates from

the fact that the second carrier only measures the motion of the input test mass (ITM) which is *local* motion in the proper frame of the beam splitter and does not contain gravitational-wave signal. One might ask: "how can we recover the detector sensitivity if the second carrier measures something that does not contain the signal?" Interestingly, even though no signal is measured by the second carrier, it measures the radiation-pressure noise of ITM introduced by the first carrier which has a much higher optical power due to the amplification of the arm cavity, as shown schematically by the flow chart of Fig. 12. By combining the outputs of two carriers optimally, we can cancel some part of the radiation-pressure noise and enhance the sensitivity—the local-readout scheme can therefore be viewed as a noise-cancelation scheme. The cancelation efficiency is only limited by the radiation-pressure noise of the second carrier.

To evaluate the sensitivity for this scheme rigorously, one has to treat the input test mass (ITM) and end test mass (ETM) individually, instead of assuming a single reduced mass as we did for those schemes mentioned earlier. One can refer to [10] for details.

3   Numerical Optimization

In this section, we will show the detail of numerical optimizing sensitivities of those schemes introduced in the previous section.

3.1   Including the classical noises
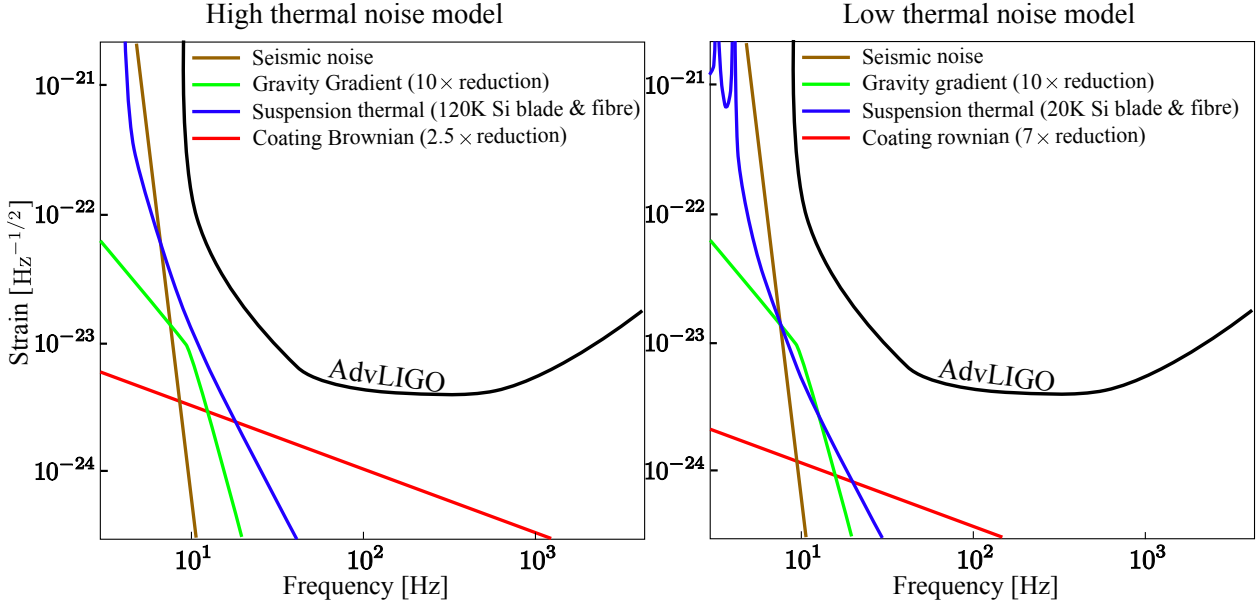
Figure 13: Plot showing the high classical noise model (left) and the low classical noise model (right).

For optimization, we also take into account the various classical noises (also called the classical noises distinguished from the quantum noise). The dominant classical noises in the detection frequency band are (i) the *seismic noise* arising from the ground motion; (ii) the *gravity gradient noise* due to the Newtonian gravity from inhomogeneous distribution of matter around the test mass; (iii) the *suspension thermal noise* originating from the random thermal fluctuation of the suspension wire; (iv) the *coating thermal noise* due to thermal fluctuation of the coating. In order for the advanced schemes to have any meaningful improvements over AdvLIGO, those classical noises have to be lower than the design specification of AdvLIGO. We assume two noise models: (i) the *high* classical noise model—-10 × reduction of the gravity gradient noise, cryogenic 120K Si suspension, and 2.5 × reduction (in strain) of the coating thermal noise; (ii) the *low* classical noise model—10 × reduction of the gravity gradient noise, cryogenic 20K Si suspension, and 7 × reduction of the coating thermal noise. The corresponding noise spectrum for these two models are shown in Fig. 13. The code for generating these curves is *GWINC*.

3.2   Cost function

The final optimization result critically depends on the cost function. In the literature, optimizations have been carried out by using a cost function that is source-oriented—trying

to maximize the signal-to-noise ratio for particular astrophysical sources. Here we apply a rather different cost function, as shown in Eq. (1), that tries to maximize the *broadband* improvement over AdvLIGO. This follows the same philosophy of designing AdvLIGO which aims at a factor of 10 broadband improvement over initial LIGO.

3.3   Optimization results

When making optimization, we separate the configurations into two groups: (i) *the frequency-dependent squeezing (input filtering) group,* in which we consider adding input filter cavities to those configurations mentioned in Sec. 2; (ii) *the variational-readout (output filtering) group*, in which we consider adding output filter cavities. Note that for those multiple-carrier schemes, e.g., the local-readout scheme, the number of filter cavities is equal to the number of carrier light, and the number of optimization parameters is therefore increased proportionally. In real implementation, one might specifically design one filter cavity that is able to simultaneously filter several carrier light with different filtering parameters, and we can then reduce the number of optics.

3.3.1   Total noise spectrum

The optimization result for the *input-filtering group* has been shown at the very beginning, i.e., in Fig. 1. Notice that, in the plot, we did not show the dual-carrier scheme with both carrier light resonant in the arm cavity, and only show the local-readout scheme in which only one carrier is resonant in the arm cavity. This is due to the interesting fact that when we fix the total power of the two carriers, the optimal power for one carrier turns out to be zero—this simply recovers the single-carrier case. Admittedly, this is due to the specific cost function and the thermal-noise model that we have chosen. In general, it is not clear that this would be optimal.

The optimization result for the *output-filtering group* has been shown in Fig. 2. It is clear that the general features are identical to the input-filtering one. The only prominent difference comes from the low-frequency sensitivities. This is attributable to the susceptibility to loss of the variational readout scheme, as mentioned early in Sec. 2.3. Again, we can see that the speed meter and the local-readout scheme allows a significant improvement at low frequencies.

In Appendix A, we have listed the optimal values for the different parameters.

3.3.2   Quantum noise contribution

To manifest the quantum noise contribution to the total noise spectrum, we show only the quantum noise spectrum in Fig. 14 and Fig. 15. It is clear that only at low frequencies do these schemes differ from each other distinctively. The low-frequency classical thermal noise, to great extents, smears off the difference. Therefore, unless significant changes can be made to reduce the low-frequency thermal noise, a sound reasoning—for choosing one advanced configuration over the other as a candidate for upgrade—should be based on the additional complexity involved, as different schemes do not perform drastically different after taking
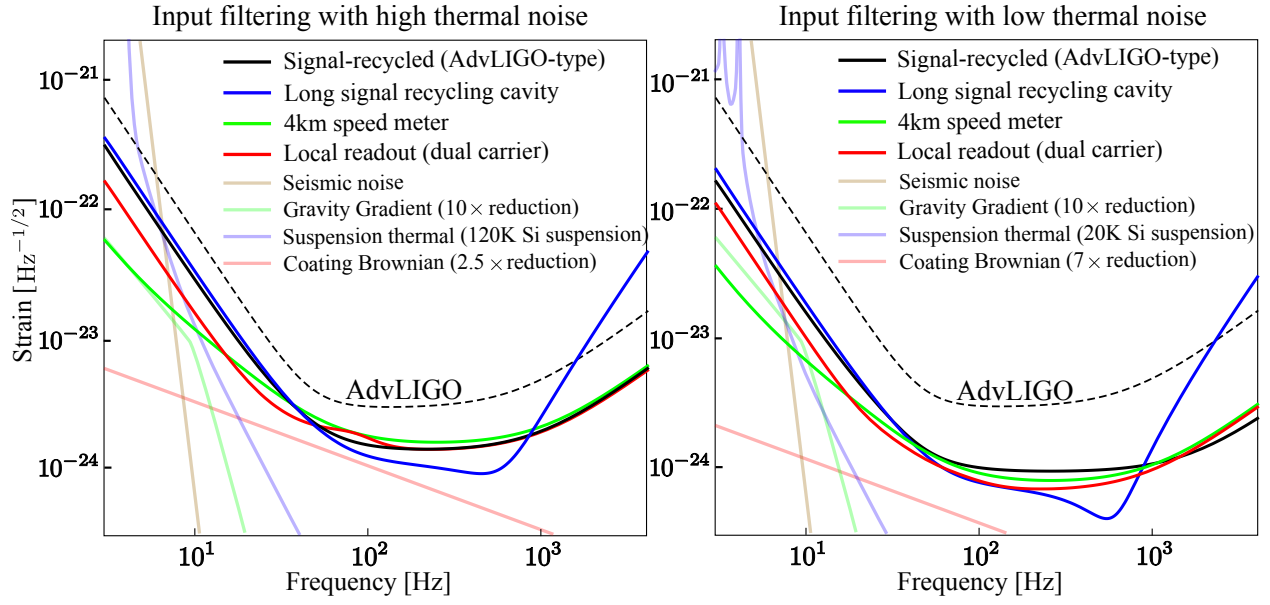
Figure 14: Plot showing the corresponding quantum noise contribution to the noise spectrum shown in Fig. 1.
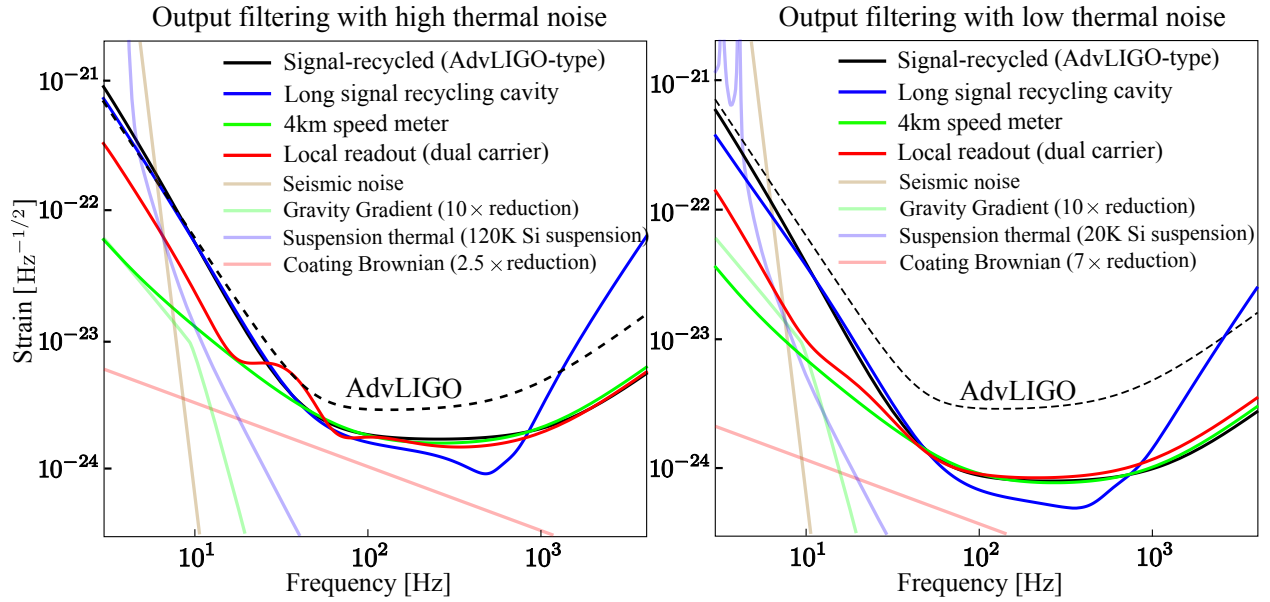
Figure 15: Plot showing the corresponding quantum noise contribution to the noise spectrum shown in Fig. 2.

into account the classical thermal noise.

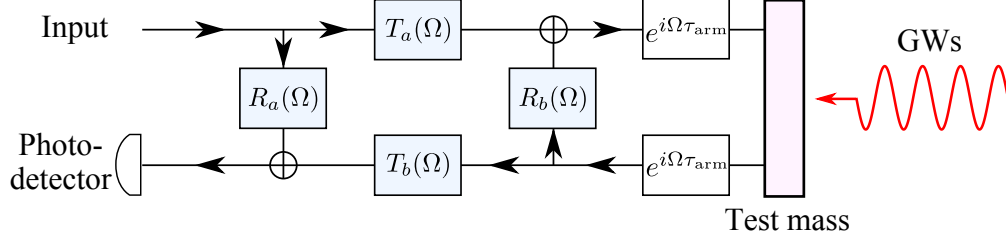**Figure 16:** Schematics illustrating the generic four-port filter that can be applied in between the test mass and the photodetector. Here we are considering one sideband frequency Ω; $\tau_{\mathrm{arm}} = L/c$ is the time delay by the interferometer arm.

4 Future study

In the current study, we only cover a few topologies among those that have been proposed in the literature. To proceed, one approach is to further expand the list of configurations, but this is a rather daunting task given the huge number of possible combinations. An alternative that we shall apply in the future is viewing optical and mechanical components as linear filters, and seeking the answer to the following question: *"What is the optimal filter that we should place in between the test mass and the photodetector such that the specific cost function is minimized or the signal-to-noise ratio is maximized if we know features of the signal spectrum?"* Similar questions have been frequently asked in designs of electronic circuits. The only subtlety is that we are dealing with quantum fluctuation — there are certain constrains on the filters that one can apply in order not to destroy the quantum coherence, especially in the case of amplitude filtering.

Being concrete, let us look at the structure of the detection process more carefully. The mirror-endowed test mass, which contains the GW signal, turns ingoing optical field into outgoing field which in turn is detected by the photodetector. In between the test mass and the photodetector, the most generic filter we can apply is a four-port filter, as illustrated in Fig. 16. The transfer functions of such a four-port filter — $T_a(\Omega)$, $T_b(\Omega)$, $R_a(\Omega)$ and $R_b(\Omega)$[1] — are not independent and need to satisfy the Stokes relation due to energy conservation and time-reversal symmetry. Specifically, if we separate their amplitude and phase shown as follows:

$$T_a(\Omega) = |T_a(\Omega)|e^{i\,\phi_a(\Omega)}, \quad T_b(\Omega) = |T_a(\Omega)|e^{i\,\phi_b(\Omega)},$$
$$R_a(\Omega) = |R_a(\Omega)|e^{i\,\varphi_a(\Omega)}, \quad R_b(\Omega) = |R_b(\Omega)|e^{i\,\varphi_b(\Omega)}, \tag{27}$$

the Stokes relation dictates the following constraints:

$$|T_a(\Omega)| = |T_b(\Omega)|, \quad |R_a(\Omega)| = |R_b(\Omega)|, \quad |T(\Omega)|^2 + |R(\Omega)|^2 = 1,$$
$$e^{i\,\phi_a(\Omega)} = e^{i\,\phi_b(\Omega)}, \quad e^{i\,\varphi_a(\Omega)+i\,\varphi_b(\Omega)} = -e^{2i\,\phi_a(\Omega)}. \tag{28}$$

In order to obtain the optimal four-port filter given a certain cost function, we can either (i) parameterize those transfer functions in terms of zeros and poles and optimize them

---

[1]For simplicity, here we use the sideband picture instead of quadrature, otherwise these transfer functions will be transfer matrices.
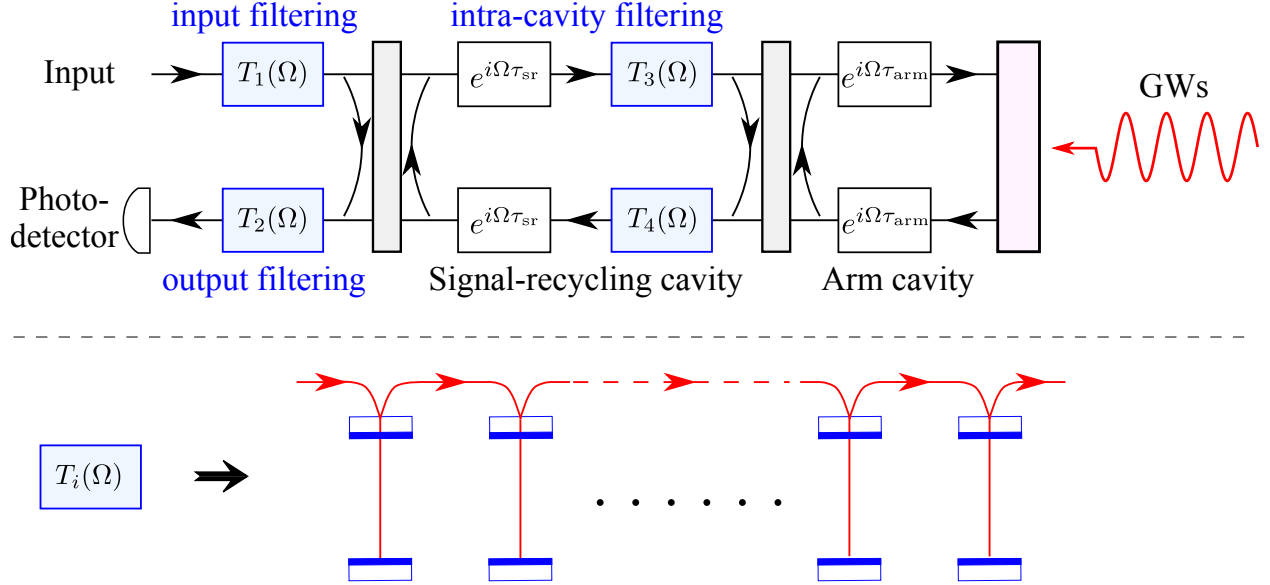
Figure 17: Schematics illustrating the scheme that we will numerically optimize (top). Each of these transfer functions corresponds to a cascade of (optomechanical) cavities in series (bottom).

— this requires mapping between zeros and poles to the physical setup, which is highly nontrivial, or (ii) insert a number of cavities and optimize the parameters — this is more transparent in terms of finding out the physical scheme. As a first attack, we will apply the latter approach, as illustrated in Fig. 17. Not only do we consider input filtering $T_1(\Omega)$ and output filtering $T_2(\Omega)$, we also include the intra-cavity filtering $T_3(\Omega)$ and $T_4(\Omega)$ — the filters sit inside the signal-recycling cavity (the sloshing cavity in the speed-meter configuration is one special example of the intra-cavity filtering). These filters are different cascades of cavities that can either have fixed mirrors (the passive cavity) or a movable end mirror (the optomechanical cavity). The usual passive optical cavity only allows us to create a frequency-dependent phase shift on the sidebands, or equivalently, frequency-dependent rotation of the amplitude and phase quadratures. By adding control light and allowing the end mirror to be movable, we can also create frequency-dependent amplitude modulation, similar to the ponderomotive squeezer proposed in Ref. [14]. Recently such active optomechanical cavity has triggered interesting discussion among the gravitational-wave community, as it allows us to filter the audio-band signal with table-top setups [15]. However, to realize it experimentally, the mirror thermal noise needs to be low enough such that the quantum coherence shall not be destroyed. This implies that cryogenic temperature is necessary which is rather challenging to realize. In the numerical optimization, we will study influence of the thermal noise in the optomechanical cavity on the sensitivity.

5 Conclusions

We have optimized the quantum noise spectrum for a few different configurations that are candidates for the 3rd generation LIGO. In particular, we have considered the frequency dependent squeezing (input filtering) and variational readout (output filtering); introducing additional filter cavities either at the input or the output ports. Limited by thermal noise at low frequencies, the difference among these configurations is not very prominent. This leads us to the conclusion that adding one input filter cavity to AdvLIGO seems to be the most feasible approach for upgrading in the near term, due to its simplicity compared with other schemes. If the low-frequency thermal noise can be reduced in the future, the speed meter and the multiple-carrier scheme can provide significant low-frequency enhancement of the sensitivity. This extra enhancement will, for some low enough thermal noise, be enough to compensate for their extra complexity.

A   Optimal Parameters

Optimal parameters for the configurations with frequency dependent squeeze angle in the high thermal noise model are listed in Table 1. The nominal parameters common among different configurations are: $m = 50$ kg, $T_{\mathrm{PRM}} = 0.03$, $T_{\mathrm{ITM}} = 0.01$ and maximal input power is equal to 125 W, which corresponds to around 1 MW circulating in the arm cavity. For the speed meter, the length of the sloshing cavity is 4 km and the power transmittance for the sloshing mirror is equal to 0.001. Note that all the configurations are tuned, as a broadband sensitivity is preferred, given the particular cost function that we have chosen.

Configurations	P_0 (W)	T_{sr}	T_f (ppm)	Δ_f (Hz)	figure of merit
Signal-recycling	125.0	0.11	245.3	-28.4	2279.2
Long signal recycling	125.0	0.17	307.0	-35.8	2142.7
Speed meter	125.0	0.04	317.7	-18.5	2324.8
Local readout (carrier A)	125.0	0.12	171.0	-19.0	2378.4
Local readout (carrier B)	120.2	0.0003	159.0	-13.6	-

Table 1: Optimal parameters for different configurations with frequency-dependent squeezing in the high thermal noise model. Here P_0 is the input optical power, T_{sr} is the power transmittance of the signal recycling mirror, T_f is the power transmittance for the front mirror of the filter cavity, Δ_f is the detune frequency of the filter cavity, and figure of merit is equal to $1000/\mathcal{C}$ with $\mathcal{C}$ the value of the cost function defined in Eq. 1—the larger the figure of merit is, the better the broadband sensitivity is.

The optimal parameters for the high thermal noise model for different configurations with frequency dependent (variational) readout quadrature are listed in the Table 2. The common parameters are the same as those for the frequency dependent squeezing.

Configurations	P_0 (W)	T_{sr}	T_f (ppm)	Δ_f (Hz)	figure of merit
Signal-recycling	125.0	0.08	207.7	-22.7	2114.5
Long signal recycling	125.0	0.10	234.5	-25.6	1970.5
Speed meter	125.0	0.27	349.2	-17.9	2301.3
Local readout (carrier A)	125.0	0.15	892.8	-22.2	2262.8
Local readout (carrier B)	26.4	0.001	907.0	-10.6	-

Table 2: Optimal parameters for different configurations with variational readout in the high thermal noise model.

The optimal parameters for different configurations with frequency dependent squeezing in the low thermal noise model are listed in the Table 3. The common parameters for different configurations are: $m = 150$kg, $T_{\mathrm{PRM}} = 0.03$, $T_{\mathrm{ITM}} = 0.01$ and maximal input power is equal to 500 W, which corresponds to approximately 3 MW intra cavity power.

The optimal parameters for the low-noise model for different configurations with frequency dependent readout quadrature are listed in the Table 4.

Configurations	P_0 (W)	T_{sr}	T_f (ppm)	Δ_f (Hz)	figure of merit
Signal-recycling	500.0	0.06	185.1	-21.8	2839.5
Long signal recycling	500.0	0.11	264.3	-30.6	2672.8
Speed meter	500.0	0.23	364.9	-21.3	2953.9
Local readout (carrier A)	500.0	0.13	260.1	-30.3	3007.9
Local readout (carrier B)	200.0	0.0005	1000	10.2	-

Table 3: Optimal parameters for different configurations with frequency-dependent squeezing in the low thermal noise model.

Configurations	P_0 (W)	T_{sr}	T_f (ppm)	Δ_f (Hz)	figure of merit
Signal-recycling	500.0	0.09	246.2	-27.6	2692.7
Long signal recycling	500.0	0.15	331.0	-37.0	2515.3
Speed meter	500.0	0.23	364.9	-21.3	2953.9
Local readout (carrier A)	317.6	0.12	237.4	-23.3	2822.6
Local readout (carrier B)	10.0	0.001	184.6	-15.3	-

Table 4: Optimal parameters for different configurations with frequency dependent readout quadrature in the low thermal noise model.

B   Basics of Quantum Noise

In this section, we will briefly review the basics for evaluating quantum noise in an interferometric gravitational-wave detection by using the input-output formalism. Additionally, we will discuss the principle behind the use of filter cavities for reducing the quantum noise. For more detail, one can refer to the review article by Danilishin and Khalili in *Living Reviews in Relativity* [?].

B.1   Input-output formalism
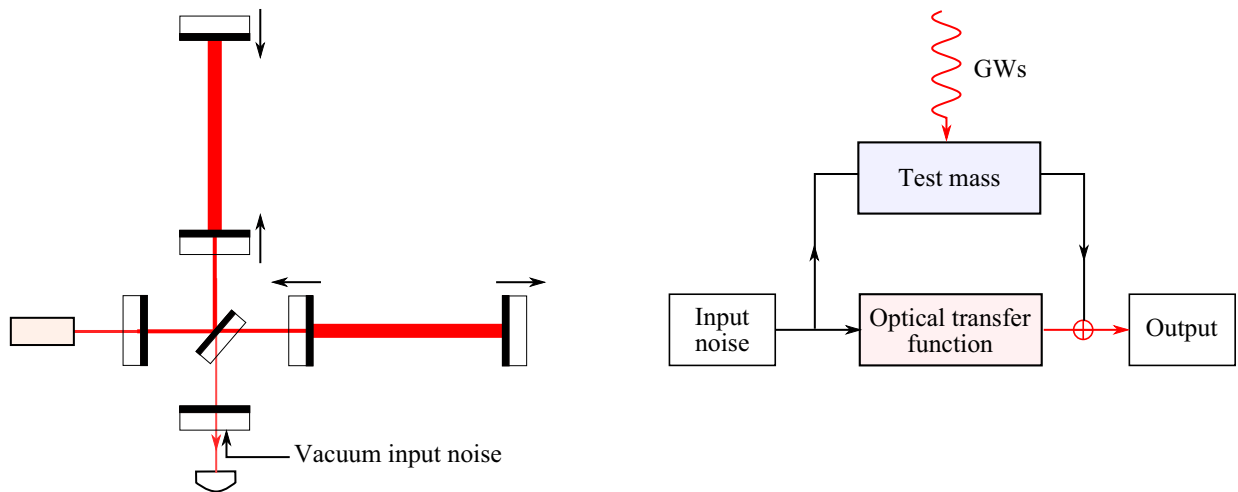
Figure 18: Schematics showing the configuration of an interferometric gravitational-wave (GW) detector (left) and the flow chart denoting the input and output (right).

When analyzing the quantum noise of an interferometric gravitational-wave detector, shown schematically in Fig. 18, the usual applied assumption is the linearity and stationarity of the system; a frequency-domain analysis can therefore be applied with the noise and signal propagating through the system via various linear transfer functions. There are two types of noise: (i) the shot noise, also called the readout noise, is the one that comes from the measurement device itself—in the context here, arising from the phase fluctuation of the light, and it usually decreases as we increase the measurement strength (the optical power). Its propagation is denoted by the lower path of the flow chart in Fig. 18 (ii) the back-action noise, also called the radiation-pressure noise here, is the one that disturbs the signal due to noise in the device, and it usually increases when the measurement strength increases. Its propagation is shown by the upper path of the flow chart in Fig. 18. In general, these two types of noise are mixed with each other. To evaluate detector sensitivity, the key is then to analyze how the noise and signal propagates and to identify those transfer functions, which give the input-output relation.

For interferometric gravitational-wave detectors, the photocurrent output I_{out} that we measure is linearly proportional to a certain optical quadrature—a linear combination of the amplitude quadrature b_1 and phase quadrature b_2[2]:

$$I_{\text{out}}(\Omega) \propto b_1(\Omega) \sin\zeta + b_2(\Omega)\cos\zeta, \tag{29}$$

where we usually call ζ the readout quadrature angle and it depends on the phase of the local oscillator (the optical field that beats with the interferometer output). In terms of amplitude and phase quadratures, the input-output relation can generally be put into the following form:

$$\left[\begin{array}{c} b_1(\Omega) \\ b_2(\Omega) \end{array}\right] = \left[\begin{array}{cc} M_{11}(\Omega) & M_{12}(\Omega) \\ M_{21}(\Omega) & M_{22}(\Omega) \end{array}\right] \left[\begin{array}{c} a_1(\Omega) \\ a_2(\Omega) \end{array}\right] + \left[\begin{array}{c} v_1(\Omega) \\ v_2(\Omega) \end{array}\right] h(\Omega). \tag{30}$$
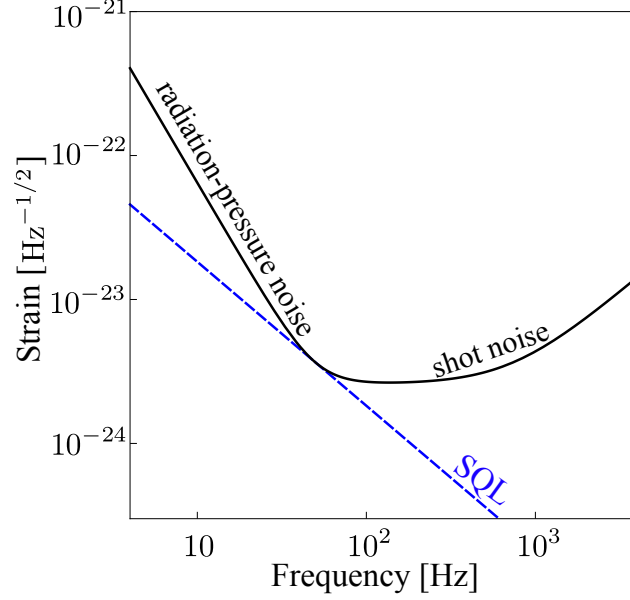
Here $\Omega = 2\pi f$ is the angular frequency; $b_1(a_1)$ and $b_2(a_2)$ are the output (input) amplitude quadrature and phase quadrature, respectively; M_{ij} are the elements of the transfer matrix, which depends on the specific optical configuration; v_i quantify the detector response to the gravitational-wave strain h. Different configurations will have different transfer matrices and response functions to the gravitational-wave signal—thus different input-output relations. In the following sections, we will see an interesting zoo of them. Once we know the input-output relation and the readout quadrature angle ζ, it then becomes rather straightforward to evaluate the detector sensitivity which is quantified by the noise spectral density [3] (normalized with respect to the signal):

$$S_h(\Omega) = \frac{(\sin\zeta \ \cos\zeta)\mathbf{M}\,\mathbf{S}\,\mathbf{M}^\dagger(\sin\zeta \ \cos\zeta)^{\text{T}}}{(\sin\zeta \ \cos\zeta)\boldsymbol{v}\boldsymbol{v}^\dagger(\sin\zeta \ \cos\zeta)^{\text{T}}}, \tag{31}$$

where $\mathbf{S}$ is the noise spectral-density matrix for the input amplitude quadrature a_1 and the phase quadrature a_2—$\langle a_i(\Omega)a_j^\dagger(\Omega')\rangle_{\text{sym}} \equiv \pi\,S_{ij}(\Omega)\delta(\Omega-\Omega')$ $(i,j=1,2)$, and in particular for non-squeezed light (vacuum) input, its elements are $S_{11} = S_{12} = 1$ and $S_{12} = S_{21} = 0$ (uncorrelated amplitude and phase noise).

---

[2]These quadratures are related to the upper sideband $b(\Omega)$ and lower sideband $b(-\Omega)$ via $b_1 = [b(\Omega) + b^\dagger(-\Omega)]/\sqrt{2}$ and $b_1 = [b(\Omega) - b^\dagger(-\Omega)]/(i\sqrt{2})$.

[3]The single-sided spectral density $S_A(\Omega)$ for any quantity A is defined through [cf. Eq. (22) in Ref. [3]]: $\langle A(\Omega)A^\dagger(\Omega')\rangle_{\text{sym}} = \frac{1}{2}\langle A(\Omega)A^\dagger(\Omega') + A^\dagger(\Omega')A(\Omega)\rangle = \frac{1}{2}2\pi S_A(\Omega)\delta(\Omega-\Omega')$.

Figure 19: The quantum-noise spectral density $S_h^{1/2}$ for a tuned interferometer given the same specification of AdvLIGO—$m = 40$kg and $P_c = 800$kW.

Take a tuned interferometer (a close model for the tuned operational mode of AdvLIGO) for instance, as shown in Ref. [3], the input-output relation is given by:

$$\begin{bmatrix} b_1(\Omega) \\ b_2(\Omega) \end{bmatrix} = e^{2i\phi} \begin{bmatrix} 1 & 0 \\ -\mathcal{K}(\Omega) & 1 \end{bmatrix} \begin{bmatrix} a_1(\Omega) \\ a_2(\Omega) \end{bmatrix} + e^{i\phi} \begin{bmatrix} 0 \\ \sqrt{2\mathcal{K}(\Omega)} \end{bmatrix} \frac{h(\Omega)}{h_{\text{SQL}}}. \tag{32}$$

We have introduced:

$$\phi \equiv \arctan(\Omega/\gamma), \quad \mathcal{K}(\Omega) \equiv \frac{2\gamma\,\iota_c}{\Omega^2(\Omega^2 + \gamma^2)}, \quad h_{\text{SQL}} \equiv \sqrt{\frac{8\hbar}{m\Omega^2 L^2}} \tag{33}$$

with γ the arm cavity bandwidth, L the length of arm cavity, parameter $\iota_c \equiv 8\omega_0 P_c/(mLc)$, ω_0 the laser frequency, and P_c the intra-cavity power. If we measure the phase quadrature by choosing the quadrature angle $\zeta = 0$, the corresponding noise spectral density will be:

$$S_h(\Omega) = \left[\mathcal{K}(\Omega) + \frac{1}{\mathcal{K}(\Omega)}\right] \frac{h_{\text{SQL}}^2}{2} \geq h_{\text{SQL}}^2 = \frac{8\hbar}{m\Omega^2 L^2}. \tag{34}$$

The first term, proportional to the optical power ($\mathcal{K} \propto P_c$), is the radiation-pressure noise and comes from the fluctuation of the input amplitude quadrature a_1; the second term, inversely proportional to the optical power, is the shot noise and comes from the fluctuation of the input phase quadrature a_2. In this simple scenario, the sensitivity is limited by the standard quantum limit (SQL)—the benchmark for the strength of quantum noise [12]. In Fig. 19, we plot $S_h^{1/2}(\Omega)$—the radiation-pressure noise dominates at low frequencies and the shot noise dominates at high frequencies.

C Optical loss and optimal filter cavity length

It is essential to gain a full understanding—through experiments and numerical modelings—of how the optical loss scales as the cavity length, and this will determine the cavity length for achieving the optimal sensitivity. Here we will provide a qualitative estimate of the dependence of sensitivity on the optical loss and the cavity length, the connection between which is left for further investigation.

Given a filter cavity, the quantum coherence, or equivalently the detector sensitivity, is affected by the total loss of the cavity $\mathcal{E}$ which is equal to the round-trip loss ϵ multiplied by the number of bounce $N \sim 2/T_f$ with T_f being the transmittance of the cavity input mirror (assuming a totally reflected end mirror), namely

$$\mathcal{E} \approx 2\epsilon/T_f. \tag{35}$$

In addition, since the filter cavity bandwidth γ_f needs to be comparable to the detection bandwidth γ of the interferometer in order to reduce the quantum noise, we require $\gamma_f = cT_0/(4L_f) \approx \gamma$, where L_f is the filter cavity length. It follows that

$$T_f \approx 4\gamma L_f/c. \tag{36}$$

Therefore, the total optical loss is given by:

$$\mathcal{E} \approx \frac{c\,\epsilon}{2\gamma L_f} \propto \frac{\epsilon}{L_f}, \tag{37}$$

which means that the total optical loss depends on the ratio between the round-trip loss and the filter cavity length. If the loss is independent of the cavity length—usually not the case, a long filter cavity can relax the requirement on the round-trip optical loss. In general, to determine the optimal cavity length, we have to work out the dependence of the round-trip optical loss on the cavity length.

References

[1] T. Corbitt and N. Mavalvala, "Review: Quantum noise in gravitational-wave interferometers," *Journal of Optics B: Quantum and Semiclassical Optics*, **6**, no. 8, S675, 2004.

[2] R. Adhikari, G. Mueller, N. Robertson, D. McClelland, Y. Chen, S. Waldman, K. Arai, and G. Harry, "LSC Instrument Science White Paper," *LIGO Document: T1100309*, 2011.

[3] H. J. Kimble, Y. Levin, A. B. Matsko, K. S. Thorne, and S. P. Vyatchanin, "Conversion of conventional gravitational-wave interferometers into quantum nondemolition interferometers by modifying their input and/or output optics," *Phys. Rev. D*, **65**, 022002, 2001.

[4] S. P. Vyatchanin and E. A. Zubova, "Quantum variation measurement of a force," *Physics Letters A*, **201**, pp. 269–274, May 1995.

[5] F. Y. Khalili and Y. Levin, "Speed meter as a quantum nondemolition measuring device for force," *Phys. Rev. D*, **54**, 004735, 1996.

[6] P. Purdue, "Analysis of a quantum nondemolition speed-meter interferometer," *Phys. Rev. D*, **66**, 022001, 2002.

[7] P. Purdue and Y. Chen, "Practical speed meter designs for quantum nondemolition gravitational-wave interferometers," *Phys. Rev. D*, **66**, 122004, 2002.

[8] Y. Chen, "Sagnac interferometer as a speed-meter-type, quantum-nondemolition gravitational-wave detector," *Phys. Rev. D*, **67**, 122004, 2003.

[9] H. Rehbein, H. Mueller-Ebhardt, K. Somiya, S. L. Danilishin, R. Schnabel, K. Danzmann, and Y. Chen, "Double optical spring enhancement for gravitational-wave detectors," *Phys. Rev. D*, **78**, 062003, 2008.

[10] H. Rehbein, H. Mueller-Ebhardt, K. Somiya, C. Li, R. Schnabel, K. Danzmann, and Y. Chen, "Local readout enhancement for detuned signal-recycling interferometers," *Phys. Rev. D*, **76**, pp. 062002–, Sept. 2007.

[11] A. Buonanno and Y. Chen, "Scaling law in signal recycled laser-interferometer gravitational-wave detectors," *Phys. Rev. D*, **67**, 062002, 2003.

[12] V. B. Braginsky and F. Y. Khalili, *Quantum Measurement.* Cambridge University Press, 1992.

[13] A. Wade, K. Mckenzie, Y. Chen, D. Shaddock, J. Chow, and D. McClelland, "A Polarization Speed Meter for Gravitational-Wave Detection," *LIGO Document: P1100205*, 2011.

[14] T. Corbitt, Y. Chen, F. Khalili, D. Ottaway, S. Vyatchanin, S. Whitcomb, and N. Mavalvala, "Squeezed-state source using radiation-pressure-induced rigidity," *Phys. Rev. A*, **73**, pp. 023801–, Feb. 2006.

[15] C. Zhao and et al. *In preparation*, 2012.